Local characterization and engineering of proximitized correlated states in graphene/$NbSe_2$ vertical heterostructures

Zhiming Zhang,[1] Kenji Watanabe,[2] Takashi Taniguchi,[3] and Brian J. LeRoy[1,*]

[1]*Physics Department, University of Arizona, 1118 E 4th Street, Tucson, Arizona 85721, USA*

[2]*Research Center for Functional Materials, National Institute for Materials Science, Namiki 1-1, Tsukuba, Ibaraki 305-0044, Japan*

[3]*International Center for Materials Nanoarchitectonics, National Institute for Materials Science, Namiki 1-1, Tsukuba, Ibaraki 305-0044, Japan*

(Received 6 May 2020; revised 15 July 2020; accepted 29 July 2020; published 26 August 2020)

Using a van der Waals (vdW) vertical heterostructure consisting of monolayer graphene, monolayer hBN and $NbSe_2$, we have performed local characterization of induced correlated states in different configurations. At a temperature of 4.6 K, we have shown that both superconductivity and charge density waves can be induced in graphene from $NbSe_2$ by proximity effects. By applying a vertical magnetic field, we imaged the Abrikosov vortex lattice and extracted the coherence length for the proximitized superconducting graphene. We further show that the induced correlated states can be completely blocked by adding a monolayer hBN between the graphene and the $NbSe_2$, which demonstrates the importance of the tunnel barrier and surface conditions between the normal metal and superconductor for the proximity effect.

DOI: 10.1103/PhysRevB.102.085429

I. INTRODUCTION

When a normal metal is placed in good contact with a superconductor, Cooper pairs can be induced in the normal metal through the proximity effect [1–3]. Because of the unique geometry and electronic structure of graphene [4], recently there has been a significant interest on inducing correlated states such as superconductivity in this relativistic quantum system [5–14]. Graphene exhibits low contact resistance and weak scattering when connected to superconductor electrodes [15,16], making it an ideal candidate for probing proximity effects. The gate tunability and the unique Dirac electrons in graphene have enabled interesting physics phenomenon such as specular Andreev reflection [17–20], Klein-like tunneling [21], and the interplay between Andreev states with quantum hall states [22,23]. Furthermore, superconducting graphene has been proposed to be a building block for hosting Majorana modes [24–27] and facilitating future topologically protected quantum computation schemes [28].

The advances of van der Waals fabricating techniques [29,30] have allowed researchers to create atomically sharp interfaces between graphene and other 2D materials. One of the ideal candidates for making a graphene-superconductor junction is $NbSe_2$, a two-dimensional material with both superconductivity and charge density wave (CDW) transitions at low temperatures [31,32]. Although several electrical transport experiments have already been performed with heterostructure devices made of graphene and $NbSe_2$ [19,23,33–35], there is still a lack of local spectroscopic and topographic information for this heterostructure. In this study, we use scanning tunneling microscopy and spectroscopy to directly probe the superconducting gap, doping level, CDWs, and vortex lattices in a graphene-$NbSe_2$ vertical heterostructure. Furthermore, with the insertion of a monolayer hBN (MLhBN) between the hBN and $NbSe_2$, we have found that the correlated states can be completely blocked.

II. EXPERIMENTAL DETAILS

To fabricate our device, graphene and hBN were mechanically exfoliated from bulk crystals and deposited on 285-nm- and 90-nm-thick SiO_2 wafers, respectively. The MLhBN was identified under an optical microscope with 590-nm monochromatic light to optimize the contrast [36]. The $NbSe_2$ flake with a thickness of ~45 nm was exfoliated inside a glovebox environment with oxygen level <1 ppm. The thickness of $NbSe_2$ was determined by an AFM inside the glovebox, the flake can be regarded as bulk sample due to its thickness [37]. The vdW heterostructure was created with a dry transfer technique [29] inside the glovebox and the $NbSe_2$ is encapsulated by the graphene and a thick hBN flake to prevent it from oxidizing. The heterostructure was fabricated such that the MLhBN partially covered the $NbSe_2$, giving a region where graphene was in direct contact with $NbSe_2$ and another region where they were separated by a monolayer of hBN. 5nm-Cr/ 50nm-Au contacts were created with electron-beam lithography and physical vapor deposition. The sample was annealed under vacuum to remove chemical residues and contaminations before putting into the STM, the relative angles between the flakes became stable once the sample was annealed. The optical image of the completed device is shown in Fig. 1(a), where the gray and blue dashed lines indicate the graphene (G) and MLhBN respectively.

STM/STS measurements were performed in an ultrahigh-vacuum LT-STM (Omicron) operating at 4.6 K, Fig. 1(b)

*leroy@arizona.edu

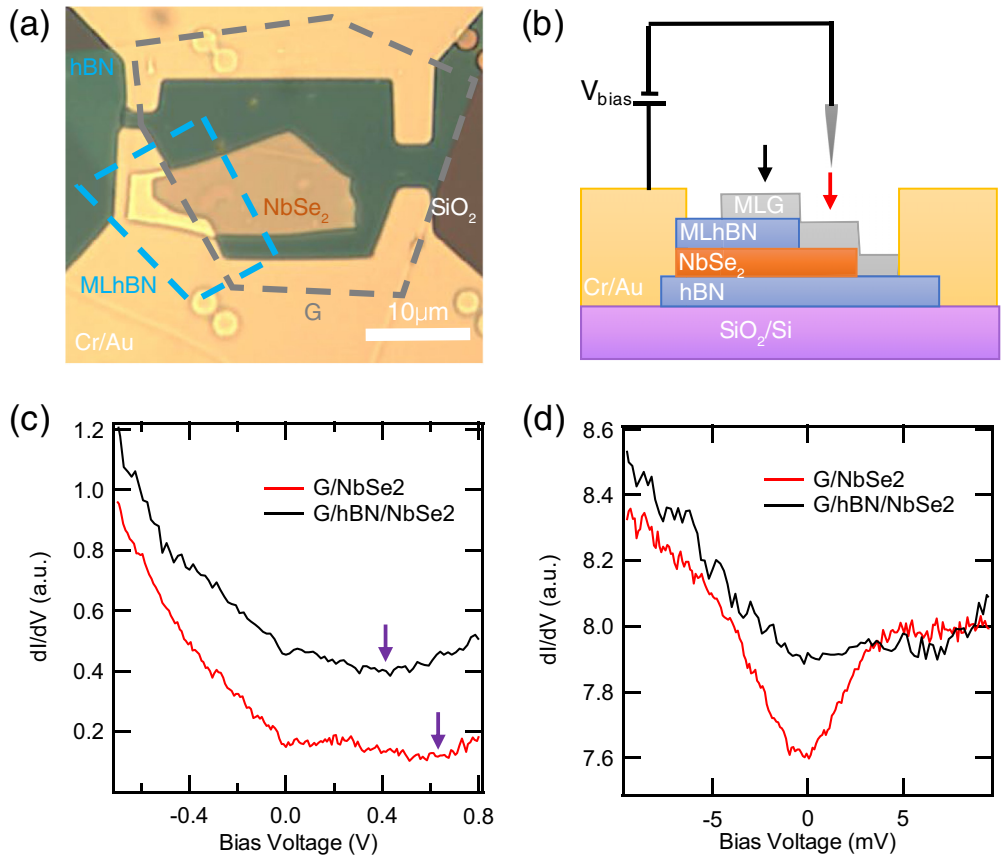

FIG. 1. (a) Optical microscopy image of the measured device. Gray and blue dashed lines enclose the monolayer graphene and monolayer hBN flakes. (b) Schematic of the STM experimental setup, black and red arrows indicated the position where the dI/dV curves in (c) and (d) were taken. (c) dI/dV spectra acquired with I = 100 pA and $V_{\mathrm{mod}} = 5$ mV. (d) dI/dV spectra acquired with I = 500 pA and $V_{\mathrm{mod}} = 0.4$ mV.

shows a schematic of the experimental setup. dI/dV spectroscopies were acquired by adding 0.4–5 mV modulation voltages (V_{mod}) at a frequency of 617 Hz to the bias voltage and measuring the current with lock-in detection. All the tips were first checked on the Au surface to ensure that they had the proper work function based on the decay of the tunnel current with distance from the sample. In addition, dI/dV spectroscopy was performed on the Au surface to ensure that the tip had a constant density of states. A small perpendicular magnetic field was applied to the device by mounting the sample on top of a permanent magnet (D43-N52, K&J Magnetics).

III. RESULTS AN DISCUSSION

A. Dirac point and superconducting gap

Figure 1(c) shows dI/dV spectra on the two different stacking configurations as indicated by the black and red arrows in Fig. 1(b). For both areas, the spectra show an overall V-shaped graphene density of states feature and the graphene is hole-doped. The Dirac point of the graphene is at ∼0.65 V in the G/$NbSe_2$ area, and ∼0.43 V in the G/hBN/$NbSe_2$ area, as indicated by the purple arrows. This is because the MLhBN lowers the work function [38] of the heterostructure under the graphene, making the graphene less *p*-doped. Beyond changing the work function, the insertion of MLhBN increases the spacing between the graphene and $NbSe_2$ layers, effectively increasing the barrier between the layers.

Figure 1(d) shows high-resolution spectroscopy on the two stacking configurations near the Fermi level. There is a soft gap opened near the Fermi level in the G/$NbSe_2$ area but not in the G/hBN/$NbSe_2$ area, indicating that the graphene directly sitting on the $NbSe_2$ area becomes superconducting as predicted by theory [39], while the graphene remains normal when there is the MLhBN between the graphene and the superconducting $NbSe_2$. The soft gap we observed here deviates from the U-shaped spectra from BCS theory [40] due to the finite temperature and disorder effect [41]. From the tunneling model of the superconducting proximity effect [2], the induced superconductivity depends on the barrier height between the superconductor and the normal metal. In our case, the insertion of a MLhBN not only induces an additional atomic layer of hBN but also creates different interfaces between the materials, thus increasing the barrier height between the graphene and $NbSe_2$ and making the induced gap not observable under our experimental conditions.

B. Determination of stacking configurations

By taking high-resolution topography images of different areas of the device, we can determine the stacking orientations from the moiré pattern formed between the different lattices. Figures 2(a), 2(c), and 2(e) show topography images

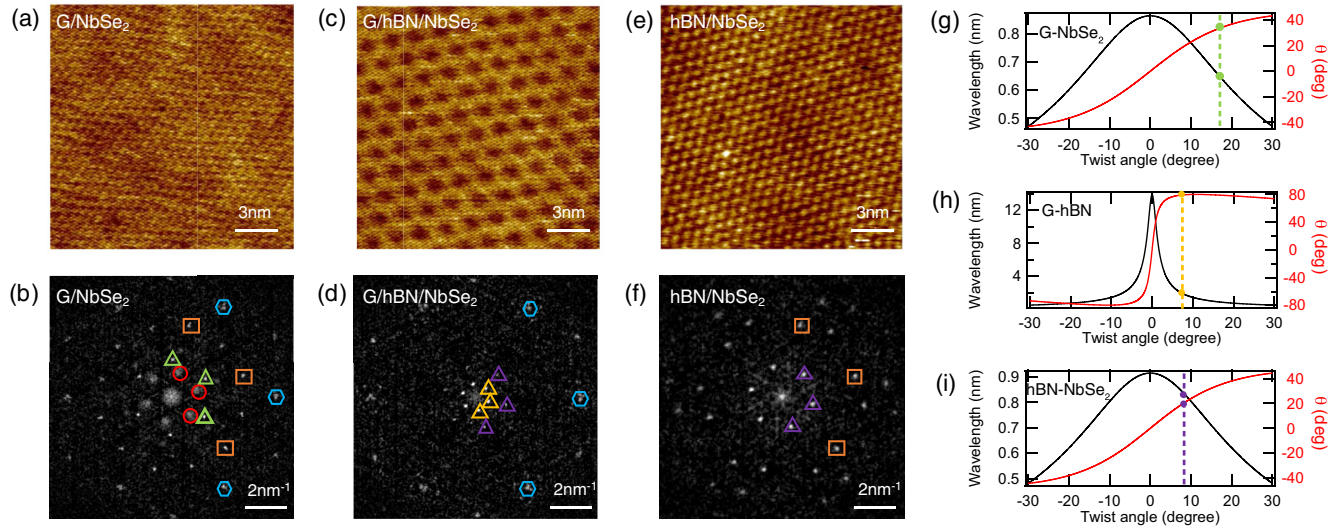

FIG. 2. [(a), (c), and (e)] Topography images of the three different stacking configurations, acquired with $V_{bias} = 0.3$ V, I = 100 pA. [(b), (d), and (f)] Symmetrized Fourier transform of (a), (c), and (e). Blue hexagons and orange rectangles mark the graphene and $NbSe_2$ lattices; red circles mark the charge density waves; green, yellow, and purple triangles mark the graphene-$NbSe_2$, graphene-hBN, and hBN-$NbSe_2$ moiré, respectively. [(g)−(i)] Theory calculation of moiré wavelengths and θ for three different configurations, colored dots indicate the experimental values and dashed lines indicate the obtained twist angle.

of the three different stacking configurations from the same device as shown in Fig. 1(a), which are: graphene on $NbSe_2$ ($G/NbSe_2$), graphene on MLhBN on $NbSe_2$ ($G/hBN/NbSe_2$) and MLhBN on $NbSe_2$ ($hBN/NbSe_2$). Figures 2(b), 2(d), and 2(f) are the Fourier transforms of the corresponding topography images. Due to the hexagonal symmetry of the lattices, we have employed a sixfold symmetrization procedure [42] to increase the signal-to-noise ratio in our Fourier transforms. Blue hexagons and orange rectangles mark the graphene and $NbSe_2$ lattices, respectively. Colored triangles mark the moiré superlattices formed by the three different possible combinations of two lattices. The wavelength of the moiré pattern is given by [43]

$$\lambda = \frac{(1+\delta)a}{\sqrt{2(1+\delta)(1-\cos\phi)+\delta^2}}, \tag{1}$$

where a is the shorter lattice constant of the two lattices, δ and ϕ are the lattice mismatch and the twist angle between the two lattices. The relative angle θ of the moiré pattern with respect to the shorter lattice is given by [43]

$$\tan\theta = \frac{\sin\phi}{(1+\delta)-\cos\phi}. \tag{2}$$

Figures 2(g)–2(i) plot the wavelength and θ as a function of twist angle for all three possible combinations of two lattices. From Figs. 2(b), 2(d), and 2(f) we can measure λ and θ for three different moiré patterns and match their values on the theoretical curves in Figs. 2(g)–2(i), the colored dots are experimental values. When the measured λ and θ are aligned vertically as marked with colored dashed lines on the graph, the twist angle between different atomic layers can then be determined. The fact that graphene-$NbSe_2$ moiré pattern only shows up in the $G/NbSe_2$ area but not in $G/hBN/NbSe_2$ area indicates that the MLhBN blocks the strong electronic coupling between the graphene and the $NbSe_2$.

Red circles in Fig. 2(b) mark the charge density waves (CDWs), which have similar feature as the CDWs that have been observed in $NbSe_2$ [44]: disks in the Fourier transform that are centered at three times the wavelength of the $NbSe_2$ lattice. Such features are not obvious in the $hBN/NbSe_2$ area and not observable in the $G/hBN/NbSe_2$ area, indicating that the CDWs can be induced in graphene when the graphene is sitting directly on the $NbSe_2$, while the characteristics of the CDWs are not preserved when the electrons are tunneling through MLhBN. We didn't observe a clear CDW gap opening in our spectroscopic measurements in Figs. 1(c) and 1(d) compared to a plain $NbSe_2$ sample [45]. This is because the proximitized CDW we observed here is much weaker. By fitting the CDW peak and $NbSe_2$ lattice peak in Fig. 2(b) with Gaussian functions, we find that the amplitude ratio between the CDW peak and the $NbSe_2$ lattice peak is ∼0.47, which is much smaller than it is in plain $NbSe_2$ (∼3) [45].

C. Vortices in graphene on $NbSe_2$

To further study the properties of the induced superconductivity in graphene, we apply a 0.26-T magnetic field perpendicular to the sample and investigate the vortices that form in the $G/NbSe_2$ area. Figure 3(a) shows a local density of states (LDOS) map measured by fixing V_{bias} at −3 mV and scanning over the sample area while recording dI/dV as a function of real-space position. From the image, we can clearly see the emergence of Abrikosov vortices [46], providing further evidence that the superconductivity is induced in the graphene by the underlying $NbSe_2$.

Figure 3(b) shows multiple dI/dV spectroscopies measured at different distances from the center of the vortex along the line indicated by the blue arrow in Fig. 3(a), the

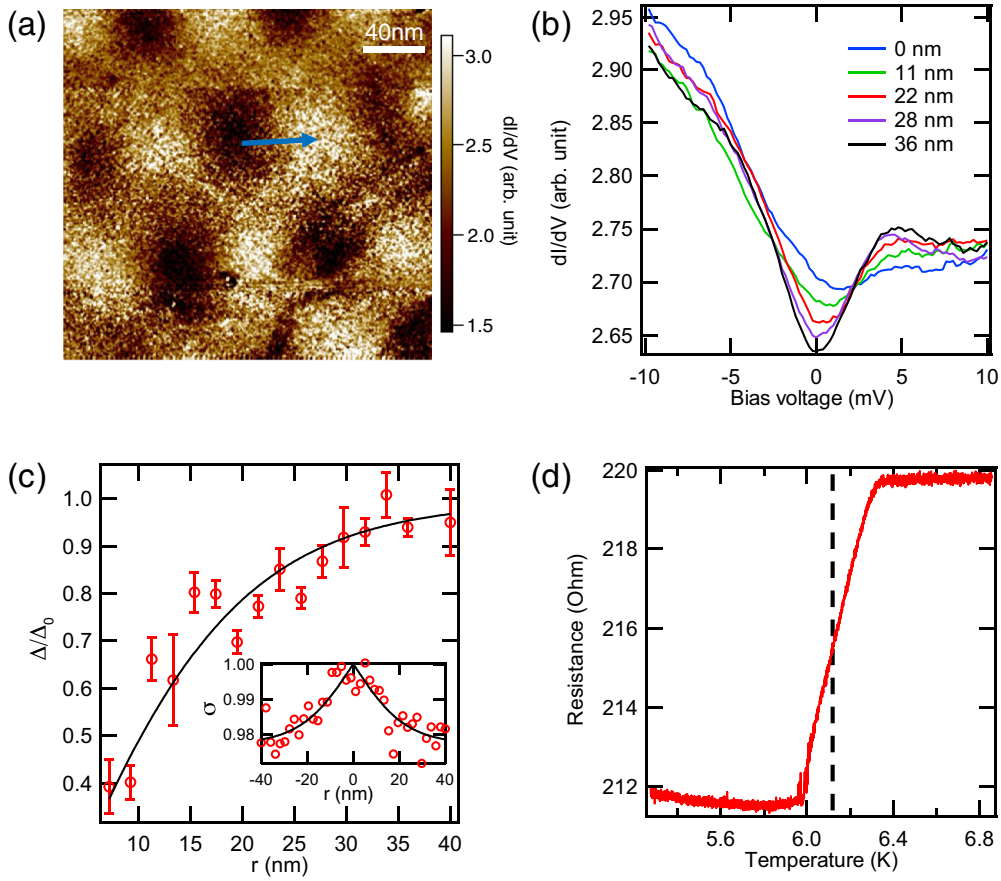

FIG. 3. (a) dI/dV map showing the vortices in graphene/$NbSe_2$ area, acquired with $V_{bias} = -3$ mV, $I = 200$ pA, and $V_{mod} = 0.4$ mV. Blue arrow indicates the position where the line cut spectroscopy were taken. (b) dI/dV spectra at different distances from the center of a vortex, acquired with $I = 500$ pA and $V_{mod} = 0.4$ mV. (c) Extracted superconducting gap plotted against the distance from the vortex center, black curve indicates the fitting function. (Inset) Normalized zero bias conductance plotted against the distance from the vortex center, black curve indicates the fitting function. (d) Two terminal resistance measurement as a function of temperature, dashed line corresponding to the critical temperature.

superconducting gap centered around the Fermi level becomes smaller and the quasiparticle peak at around 4 mV is weaker when it is closer to the center of the vortex. The asymmetry of the spectra is from the fact that the Dirac point is higher in energy than the Fermi level and the superconducting gap is superimposed on the graphene density of states.

To see how the superconducting gap changes as a function of distance from the vortex center, we fit each dI/dV spectroscopy curve and extract the superconducting gap. At zero temperature, the Dynes formula [41] is given by

$$\rho(E,\Gamma) = \rho_0 \mathrm{Re}\left[\frac{E - i\Gamma}{(E - i\Gamma)^2 - \Delta^2}\right]. \tag{3}$$

where ρ is the density of states, ρ_0 is the normal-state density of states at the Fermi level, Γ accounts for the broadening effects other than temperature. To include the finite temperature effects, we integrate the density of states with the derivative of the Fermi-Dirac distribution f, the measured density of states N is then given by

$$N(V) = N_g \int_{-\infty}^{\infty} dE \left(-\frac{\partial f}{\partial E}\right) \rho(E + eV, \Gamma). \tag{4}$$

In the above equation, N_g is the background density of states, accounting for the asymmetric density of states induced by the presence of doped graphene and possibly also tip effects, we use a two-segment linear function to model this factor:

$$N_g(V) = \begin{cases} N_0 + \alpha V & V < 0 \\ N_0 + \beta V & V \geqslant 0 \end{cases}, \tag{5}$$

where N_0, α, and β are constants.

Figure 3(c) shows the extracted superconducting gap as a function of the distance from the vortex center r. The superconducting gap far away from the vortex Δ_0 was determined by the two-terminal temperature dependent resistance measurement shown in Fig. 3(d). We define the measured critical temperature T_C as the midpoint of the step transition, then Δ_0 was calculated by using the equation [40]: $\Delta_0 = 1.764 k_B T_C$. For our device, we have obtained that $T_C \sim 6.1$ K and $\Delta_0 = 0.93$ meV, which is ~85% percent of the value for a bulk $NbSe_2$ crystal [31]. This ratio describes the quality of the interface between the normal graphene and the superconducting $NbSe_2$. Our reduction in T_C is comparable to another experiment when aluminum was directly deposited

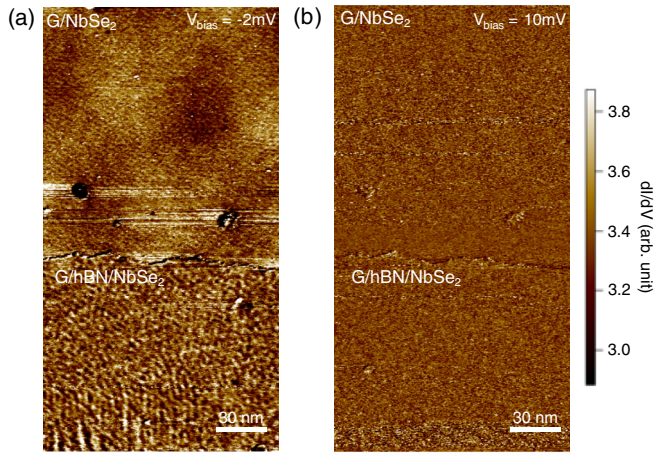

FIG. 4. (a) dI/dV map under a perpendicular magnetic field around the monolayer hBN edge, acquired with $V_{\text{bias}} = -2\,\text{mV}$, $I = 200\,\text{pA}$, and $V_{\text{mod}} = 0.4\,\text{mV}$. (b) Same image as (a) except acquired with $V_{\text{bias}} = 10\,\text{mV}$.

on graphene [20], indicating that a high-quality interface was achieved by our sample fabrication process.

Another parameter that can represent the interface quality between a type II superconductor and normal metal is the coherence length ξ, which is expected to increase for decreasing interface transparency [47]. We use the following equation [48] to obtain the coherence length from the extracted superconducting gap:

$$\frac{\Delta}{\Delta_0}(r) = \tanh\left(\frac{r}{\xi}\right), \tag{6}$$

from the fitting curve in Fig. 3(d) we have obtained that $\xi = (18.6 \pm 0.4)$ nm. An alternate way of extracting the coherence is by fitting the zero-bias conductance (ZBC) line profile crossing the center of the vortex, with the equation given by [49]

$$\sigma(r, 0) = \sigma_0 + (1 - \sigma_0)\left[1 - \tanh\left(\frac{r}{\sqrt{2}\xi}\right)\right], \tag{7}$$

where σ is the normalized ZBC and σ_0 is the normalized ZBC away from the vortex center. The insert of Fig. 3(c) shows the normalized ZBC data and the fitting results, giving $\xi = (23.2 \pm 6.6)$ nm. The coherence lengths that we have obtained from two different methods agree with each other and they are comparable to the previously reported coherence length (7.7 to 28.2 nm) for bulk $NbSe_2$ [49–52], which further confirms that our graphene is in good contact with $NbSe_2$.

D. Scattering waves

In Fig. 1(d), we have shown that the superconducting gap is not present for the G/hBN/$NbSe_2$ area, we further confirm this by imaging the LDOS near the MLhBN edge in the presence of an external magnetic field, as shown in Fig. 4, the upper area is the G/$NbSe_2$ area and the lower area is the G/hBN/$NbSe_2$ area. When imaging close to the superconducting gap, $V_{\text{bias}} = -2\,\text{mV}$, from Fig. 4(a), we can see that the Abrikosov vortices are only present in the upper area, consistent with our spectroscopic data. Additionally, we observed long-wavelength scattering waves in the lower area, similar to those observed in graphene near an atomic step edge [53,54] or near defects [55]. When imaging at a higher voltage, $V_{\text{bias}} = 10\,\text{mV}$, both the vortices and the scattering waves are gone, as shown in Fig. 4(b), since the amplitude of the scattering waves in graphene decay very fast with energy [53].

The scattering waves can be used to determine the dispersion of the material. We measure the LDOS maps at different energies in an area close to many surface defects so that the scattering waves are strong. Figures 5(a), 5(c), and 5(e) are selected LDOS images taken at negative tip voltage, close to the Fermi level and positive tip voltage. Figures 5(b), 5(d), and 5(f) are the Fourier transforms of the above images, the disk-like feature at the center is due to intravalley scattering process [42]. Its size shrinks as the wavelength of electrons becomes longer and therefore by measuring its diameter as a function of tip voltage, we can obtain the energy versus momentum dispersion relation. Figure 5(g) shows the wavevectors of the scattering waves measured from the Fourier transform images, as expected from the graphene band structure, it can be fit with a linear equation [53]:

$$k(V) = \frac{2}{\hbar v_f}(eV - eV_0), \tag{8}$$

where e is the charge of an electron, V_0 is the position of the Dirac point, v_f is the fermi velocity of the electrons. From the fitting we obtained that $V_0 = (437 \pm 15)$ meV, consistent with the Dirac point obtained from our spectroscopy data in Fig. 1(c). The fitted $v_f = (1.00 \pm 0.03) \times 10^6$ m/s is consistent with theory [4].

The scattering waves observed in the G/hBN/$NbSe_2$ area are identical to those observed in G/hBN heterostructures [53–55], while the absence of scattering waves in the G/$NbSe_2$ area is consistent with electrical transport measurements reporting low electronic scattering between the graphene and the superconductor when they are in contact [15,16]. The suppression of scattering waves in graphene happened simultaneously with proximity effect induced superconductivity, which can be an interesting aspect for future studies.

IV. CONCLUSIONS

In summary, we have found that both proximitized superconductivity and CDWs exist in the graphene-$NbSe_2$ heterostructure. By applying a magnetic field, we directly imaged the Abrikosov vortices in the G/$NbSe_2$ area and extracted the coherence length from the distance dependent ZBC and superconducting gap. Furthermore, by inserting a MLhBN between the graphene and the $NbSe_2$, both the CDWs and superconductivity are suppressed in graphene, which demonstrates the importance of the barrier between the normal metal and superconductor interface for proximitized effects. From the scattering waves, we have obtained the dispersion relation of the graphene on the G/MLhBN/$NbSe_2$ substrate, which is consistent with our spectroscopic study and the theory [4], the absence of scattering waves in the G/$NbSe_2$ area is consistent with transport measurements that observed low scattering [15,16]. The above observations indicate that even a monolayer of hBN is a very good barrier to block interactions between the graphene and the $NbSe_2$.

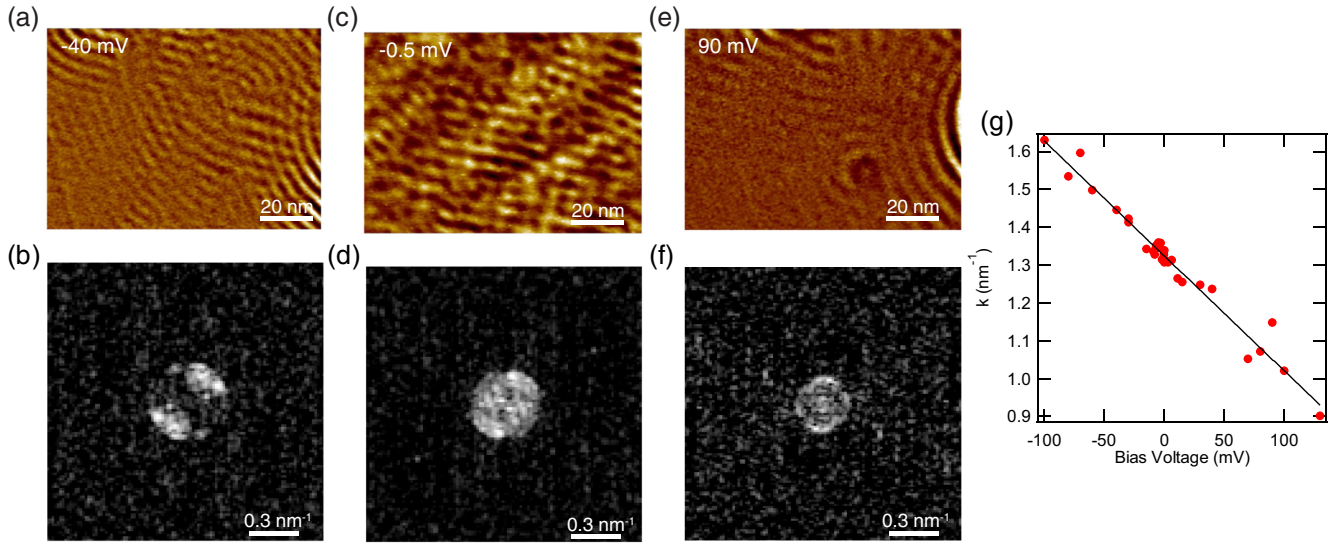

FIG. 5. (a) dI/dV map near surface defects, acquired with $V_{\text{bias}} = -40\,\text{mV}$, $I = 500\,\text{pA}$, and $V_{\text{mod}} = 3\,\text{mV}$. (b) dI/dV map acquired with $V_{\text{bias}} = -0.5\,\text{mV}$, $I = 50\,\text{pA}$, and $V_{\text{mod}} = 0.4\,\text{mV}$. (c) dI/dV map acquired with $V_{\text{bias}} = 90\,\text{mV}$, $I = 40\,\text{pA}$, and $V_{\text{mod}} = 5\,\text{mV}$. [(b), (d), and (f)] Fourier transform of (a), (c), and (e). (g) Wave vector of the scattering wave as a function of bias voltage, solid black line indicates the fitting function.

Our experiment is the first local characterization of the graphene-$NbSe_2$ heterostructure. We have demonstrated the importance of the interface barrier height for the proximitized correlated states including CDWs and superconductivity in vdW heterostructures. Moreover, we provide an innovative way to engineer the proximitized correlated states by the insertion of MLhBN, which opens the possibility of making more versatile superconducting devices and circuits in the future.

ACKNOWLEDGMENTS

The work at the University of Arizona was supported by the National Science Foundation under grant DMR-1708406 and the Army Research Office under Grant No. W911NF-18-1-0420. K.W. and T.T. acknowledge support from the Element Strategy Initiative conducted by the MEXT, Japan, Grant No. JPMXP0112101001, JSPS KAKENHI Grant Nos. JP20H00354 and the CREST (JPMJCR15F3), JST.

[1] B. D. Josephson, Phys. Lett. **1**, 251 (1962).
[2] W. L. McMillan, Phys. Rev. **175**, 537 (1968).
[3] P. G. de Gennes, Rev. Mod. Phys. **36**, 225 (1964).
[4] A. H. Castro Neto, F. Guinea, N. M. R. Peres, K. S. Novoselov, and A. K. Geim, Rev. Mod. Phys. **81**, 109 (2009).
[5] N. B. Kopnin and E. B. Sonin, Phys. Rev. Lett. **100**, 246808 (2008).
[6] B. Uchoa and A. H. Castro Neto, Phys. Rev. Lett. **98**, 146801 (2007).
[7] T. Ma, F. Yang, H. Yao, and H. Q. Lin, Phys. Rev. B **90**, 245114 (2014).
[8] J. P. L. Faye, P. Sahebsara, and D. Sénéchal, Phys. Rev. B **92**, 085121 (2015).
[9] M. L. Kiesel, C. Platt, W. Hanke, D. A. Abanin, and R. Thomale, Phys. Rev. B **86**, 020507(R) (2012).
[10] R. Nandkishore, R. Thomale, and A. V. Chubukov, Phys. Rev. B **89**, 144501 (2014).
[11] J. González, Phys. Rev. B **78**, 205431 (2008).
[12] R. Nandkishore, L. S. Levitov, and A. V. Chubukov, Nat. Phys. **8**, 158 (2012).
[13] F. D. Natterer, J. Ha, H. Baek, D. Zhang, W. G. Cullen, N. B. Zhitenev, Y. Kuk, and J. A. Stroscio, Phys. Rev. B **93**, 045406 (2016).
[14] C. Tonnoir, A. Kimouche, J. Coraux, L. Magaud, B. Delsol, B. Gilles, and C. Chapelier, Phys. Rev. Lett. **111**, 246805 (2013).
[15] V. E. Calado, S. Goswami, G. Nanda, M. Diez, A. R. Akhmerov, K. Watanabe, T. Taniguchi, T. M. Klapwijk, and L. M. K. Vandersypen, Nat. Nanotechnol. **10**, 761 (2015).
[16] M. Ben Shalom, M. J. Zhu, V. I. Fal'ko, A. Mishchenko, A. V. Kretinin, K. S. Novoselov, C. R. Woods, K. Watanabe, T. Taniguchi, A. K. Geim, and J. R. Prance, Nat. Phys. **12**, 318 (2016).
[17] C. W. J. Beenakker, Phys. Rev. Lett. **97**, 067007 (2006).
[18] D. K. Efetov, L. Wang, C. Handschin, K. B. Efetov, J. Shuang, R. Cava, T. Taniguchi, K. Watanabe, J. Hone, C. R. Dean, and P. Kim, Nat. Phys. **12**, 328 (2016).
[19] M. R. Sahu, P. Raychaudhuri, and A. Das, Phys. Rev. B **94**, 235451 (2016).
[20] L. Bretheau, J. I. J. Wang, R. Pisoni, K. Watanabe, T. Taniguchi, and P. Jarillo-Herrero, Nat. Phys. **13**, 756 (2017).
[21] D. Perconte, F. A. Cuellar, C. Moreau-Luchaire, M. Piquemal-Banci, R. Galceran, P. R. Kidambi, M. B. Martin, S. Hofmann, R. Bernard, B. Dlubak, P. Seneor, and J. E. Villegas, Nat. Phys. **14**, 25 (2018).

[22] G. H. Lee, K. F. Huang, D. K. Efetov, D. S. Wei, S. Hart, T. Taniguchi, K. Watanabe, A. Yacoby, and P. Kim, Nat. Phys. **13**, 693 (2017).
[23] M. R. Sahu, X. Liu, A. K. Paul, S. Das, P. Raychaudhuri, J. K. Jain, and A. Das, Phys. Rev. Lett. **121**, 086809 (2018).
[24] N. H. Lindner, E. Berg, G. Refael, and A. Stern, Phys. Rev. X **2**, 041002 (2012).
[25] D. J. Clarke, J. Alicea, and K. Shtengel, Nat. Commun. **4**, 1348 (2013).
[26] P. San-Jose, J. L. Lado, R. Aguado, F. Guinea, and J. Fernández-Rossier, Phys. Rev. X **5**, 041042 (2015).
[27] W. Bishara and C. Nayak, Phys. Rev. Lett. **99**, 066401 (2007).
[28] R. S. K. Mong, D. J. Clarke, J. Alicea, N. H. Lindner, P. Fendley, C. Nayak, Y. Oreg, A. Stern, E. Berg, K. Shtengel, and M. P. A. Fisher, Phys. Rev. X **4**, 011036 (2014).
[29] K. Kim, M. Yankowitz, B. Fallahazad, S. Kang, H. C. P. Movva, S. Huang, S. Larentis, C. M. Corbet, T. Taniguchi, K. Watanabe, S. K. Banerjee, B. J. LeRoy, and E. Tutuc, Nano Lett. **16**, 1989 (2016).
[30] R. Frisenda, E. Navarro-Moratalla, P. Gant, D. Pérez De Lara, P. Jarillo-Herrero, R. V Gorbachev, and A. Castellanos-Gomez, Chem. Soc. Rev. **47**, 53 (2018).
[31] H. N. S. Lee, H. McKinzie, D. S. Tannhauser, and A. Wold, J. Appl. Phys. **40**, 602 (1969).
[32] D. E. Moncton, J. D. Axe, and F. J. Disalvo, Phys. Rev. Lett. **34**, 734 (1975).
[33] M. Kim, G. H. Park, J. H. J. Lee, J. H. J. Lee, J. Park, H. H. J. Lee, G. H. Lee, and H. H. J. Lee, Nano Lett. **17**, 6125 (2017).
[34] R. Moriya, N. Yabuki, and T. Machida, Phys. Rev. B **101**, 054503 (2020).
[35] J. Li, H.-B. Leng, H. Fu, K. Watanabe, T. Taniguchi, X. Liu, C.-X. Liu, and J. Zhu, Phys. Rev. B **101**, 195405 (2020).
[36] R. V. Gorbachev, I. Riaz, R. R. Nair, R. Jalil, L. Britnell, B. D. Belle, E. W. Hill, K. S. Novoselov, K. Watanabe, T. Taniguchi, A. K. Geim, and P. Blake, Small **7**, 465 (2011).
[37] X. Xi, Z. Wang, W. Zhao, J. H. Park, K. T. Law, H. Berger, L. Forró, J. Shan, and K. F. Mak, Nat. Phys. **12**, 139 (2016).
[38] W. Auwärter, Surf. Sci. Rep. **74**, 1 (2019).
[39] Y. S. Gani, H. Steinberg, and E. Rossi, Phys. Rev. B **99**, 235404 (2019).
[40] J. Bardeen, L. N. Cooper, and J. R. Schrieffer, Phys. Rev. **108**, 1175 (1957).
[41] R. C. Dynes, V. Narayanamurti, and J. P. Garno, Phys. Rev. Lett. **41**, 1509 (1978).
[42] M. Yankowitz, D. McKenzie, and B. J. LeRoy, Phys. Rev. Lett. **115**, 136803 (2015).
[43] M. Yankowitz, J. Xue, D. Cormode, J. D. Sanchez-Yamagishi, K. Watanabe, T. Taniguchi, P. Jarillo-Herrero, P. Jacquod, and B. J. LeRoy, Nat. Phys. **8**, 382 (2012).
[44] C. J. Arguello, S. P. Chockalingam, E. P. Rosenthal, L. Zhao, C. Gutiérrez, J. H. Kang, W. C. Chung, R. M. Fernandes, S. Jia, A. J. Millis, R. J. Cava, and A. N. Pasupathy, Phys. Rev. B **89**, 235115 (2014).
[45] M. M. Ugeda, A. J. Bradley, Y. Zhang, S. Onishi, Y. Chen, W. Ruan, C. Ojeda-Aristizabal, H. Ryu, M. T. Edmonds, H.-Z. Tsai, A. Riss, S.-K. Mo, D. Lee, A. Zettl, Z. Hussain, Z.-X. Shen, and M. F. Crommie, Nat. Phys. **12**, 92 (2015).
[46] A. A. Abrikosov, Zh. Eksp. Teor. Fiz. **32**, 1442 (1957) [Sov. Phys. JETP **5**, 1174 (1957)].
[47] A. A. Golubov, Czechoslov. J. Phys. **46**, 569 (1996).
[48] F. Gygi and M. Schlüter, Phys. Rev. B **43**, 7609 (1991).
[49] J. P. Xu, C. Liu, M. X. Wang, J. Ge, Z. L. Liu, X. Yang, Y. Chen, Y. Liu, Z. A. Xu, C. L. Gao, D. Qian, F. C. Zhang, and J. F. Jia, Phys. Rev. Lett. **112**, 217001 (2014).
[50] P. de Trey, S. Gygax, and J. P. Jan, J. Low Temp. Phys. **11**, 421 (1973).
[51] J. E. Sonier, R. F. Kiefl, J. H. Brewer, J. Chakhalian, S. R. Dunsiger, W. A. Mac Farlane, R. I. Miller, A. Wong, G. M. Luke, and J. W. Brill, Phys. Rev. Lett. **79**, 1742 (1997).
[52] A. P. Volodin, A. A. Golubov, and J. Aarts, Z. Phys. B **102**, 317 (1997).
[53] J. Xue, J. Sanchez-Yamagishi, K. Watanabe, T. Taniguchi, P. Jarillo-Herrero, and B. J. LeRoy, Phys. Rev. Lett. **108**, 016801 (2012).
[54] M. Yankowitz, J. I.-J. Wang, S. Li, A. G. Birdwell, Y.-A. Chen, K. Watanabe, T. Taniguchi, S. Y. Quek, P. Jarillo-Herrero, and B. J. LeRoy, APL Mater. **2**, 092503 (2014).
[55] P. Mallet, I. Brihuega, S. Bose, M. M. Ugeda, J. M. Gómez-Rodríguez, K. Kern, and J. Y. Veuillen, Phys. Rev. B **86**, 045444 (2012).